Effect of pressure and fluid on pore geometry and anelasticity of dolomites

Wei Cheng, José M. Carcione, Stefano Picotti & Jing Ba

Rheologica Acta

ISSN 0035-4511

Rheol Acta
DOI 10.1007/s00397-020-01231-7

Springer

Rheologica Acta
https://doi.org/10.1007/s00397-020-01231-7

ORIGINAL CONTRIBUTION

Effect of pressure and fluid on pore geometry and anelasticity of dolomites

Wei Cheng[1] · **José M. Carcione**[1,2] · **Stefano Picotti**[2] · **Jing Ba**[1]

Received: 17 February 2020 / Revised: 23 July 2020 / Accepted: 3 August 2020

Abstract

The acoustic properties of rocks depend on porosity, pressure, and pore fluid and also on pore geometry. Anelasticity (attenuation and velocity dispersion) is more affected by crack aspect ratio and fraction (soft pores) than by equant (stiff) pores. To study this fact, we have performed ultrasonic measurements on two dolomite samples under variable pressure and fluid content, and used the EIAS (equivalent inclusion-average stress) model to obtain the crack aspect ratio and fraction from the bulk and shear moduli of the rock. The theory has an excellent agreement with the experimental data, and the results show that the crack attributes decrease with increasing differential pressure and are higher for a stiffer fluid. In fact, the interpretation of the experiments with the model shows that crack fraction and aspect ratio increase with the bulk modulus of the fluid (water and oil). Then, by extending the theory to all frequencies, using the Zener mechanical model, we obtain the phase velocities and quality factors as a function of frequency. Our findings reveal the importance of considering differential pressure and fluid type to analyze pore geometry and rock anelasticity.

Keywords Crack aspect ratio · Crack fraction · Anelasticity · Differential pressure · Fluid type · EIAS model · Zener model · Dolomites

Introduction

The anelastic properties of rocks—wave velocity dispersion and attenuation—have gained much attention in recent years. The applications cover a variety of fields, including geophysical prospecting, soil mechanics, and underwater acoustics. In particular, in the exploration of hydrocarbon reservoirs, it is important to predict porosity, permeability and the presence of fluids (type and saturation) (Carcione 2014). Moreover, anelasticity is closely related to the microstructural properties, fluid content, and in situ conditions, basically, pore geometry and density, and pore pressure (Jones 1986; Müller et al. 2010; Cheng et al. 2020).

Gassmann (1951) equation can be used to predict the wave velocities (Murphy 1984). However, it is only valid at the low frequency limit, due to the assumption of complete fluid pressure equilibration between cracks and stiff pores (Cleary 1978; Mavko and Nolen-Hoeksema 1994; King and Marsden 2002; Ba et al. 2016, 2017). Moreover, this equation incorporates pore geometry information through the use of empirically determined stiffnesses and therefore cannot be used to predict the dependence of the acoustic properties on the soft-pore attributes (crack aspect ratio and fraction).

In order to model the pore geometry and anelasticity of dolomites, we consider the EIAS model (Endres and Knight 1997), which is consistent with the Hashin-Shtrikman bounds when applied to two-phase systems regardless of the pore shape spectrum, and give Gassmann equation at the low frequency limit. The pore attributes (crack aspect ratio and fraction) are sensitive to differential pressure and fluid type, and affect the rock stiffnesses. Izumotani and Onozuka (2013) found that the soft pore aspect ratios and fractions of rock samples at high differential pressures are smaller than at ambient pressure. Toksöz et al. (1976) stated that the soft pores become thinner and equant (stiff) pores diminish their volume when pressure is applied. As differential pressure increases, the cracks with lower aspect ratio close first and the cracks with higher aspect ratios become slenderer until closed (Zhang et al. 2019). Cheng and Toksöz (1979) give the expression of the aspect ratio as a function of pressure and show that the crack fraction divided by the aspect ratio is constant.

✉ Jing Ba
jba@hhu.edu.cn

[1] School of Earth Sciences and Engineering, Hohai University, Nanjing 211100, China

[2] Istituto Nazionale di Oceanografia e di Geofisica Sperimentale (OGS), Borgo Grotta Gigante 42c, 34010 Sgonico, Trieste, Italy

We have performed systematic experimental observations on dolomite samples of different porosity. The tests at various confining pressures show a remarkable velocity dispersion. We use the EIAS model to study the effects of crack attributes and pressure on anelasticity at full water and oil saturation, focusing on the effects of pressure and fluid type. The original EIAS model is here extended to the whole frequency range, based on the Zener viscoelastic model (EIAS-Zener model). Fitting this model to the experimental data allows us to obtain the effective crack aspect ratio and fraction, and the frequency dependence of the phase velocities and quality factors.

Laboratory experiments

Laboratory experiments have been performed on two dolomite cylindrical specimens (24.9–25.0 mm in diameter and 37.8–44.9-mm long). The experimental setup is explained in Guo et al. (2009), which consists of a pulse generator (Panametrics 5077PR) and a digital oscilloscope (Tektronix TDS 420 A). For isolating the core from the confining pressure, the sample is jacketed with a rubber tubing. P and S waves are generated by PZT-ceramic crystals. The digitizing board in the computer is connected to the receiving transducer through a signal amplifier. The transmission and receiver transducers are located at the two ends of the sample. Each endplate includes a pore fluid inlet, which allows the passage of pore fluids through. The adopted acquisition rate is 50 M/s, the temporal resolution is 0.02 μs, and the measurement frequency is 1 MHz.

The samples (DO1 and DO2), collected from the Leikoupo formation (more than 4 km depth), in the Sichuan Basin of Southwest China and are mainly micrite and limy dolomites, made of calcite, dolomite, and clay. The ultrasonic P and S wave velocities (V_P and V_S) were measured at full water and oil saturations (water: pure water, oil: kerosene). The test has been performed under a constant pore pressure of 10 MPa and temperature of 140 °C, whereas the confining pressure increases from 20 to 80 MPa (confining pressure: 20, 25, 30, 35, 40, 45, 50, 60, 70, and 80 MPa), we use the difference between the confining pressure and the pore pressure as the differential pressure. The waveforms were acquired also for aluminum standard of the same size and shape, and velocities are obtained from the first arrivals. The P wave attenuation has been estimated by the spectral ratio method (Picotti and Carcione 2006). Table 1 shows the properties of the samples. Figure 1 shows V_P and V_S as a function of the differential pressure for full water and oil saturation. As can be seen, the velocities increase with pressure, as expected. The P wave velocity is higher for the water saturated sample, while the S wave velocity has the opposite behavior, due to the density effect (the shear modulus is approximately constant and the density decreases).

Table 1 Dry rock properties

Sample	Porosity (%)	Dry rock density (kg/m^3)	K_0 (GPa)	G_0 (GPa)
DO1	4.99	2665.86	76.4	49.7
DO2	16.87	2321.29	76.4	49.7

The intrinsic quality factor Q is calculated by using the spectral ratio method on the same set of compressional waveforms acquired from the rock sample and the standard material. Aluminum is chosen as standard medium due to its very high quality factor (Ba et al. 2019; Guo and Fu 2007; Toksöz et al. 1979). Q can be determined from

$$\ln\left(\frac{A_1(f)}{A_2(f)}\right) = -\frac{\pi x}{QV} f + \ln\frac{G_1(x)}{G_2(x)}, \tag{1}$$

where subscripts 1 and 2 denote the rock sample and standard material respectively, A is the amplitude spectrum, f is the frequency, x is the propagation distance, V is the wave velocity, and G is a geometrical factor. Thereafter, Q can be obtained from least squares fits to the slope of the natural log of $A_1(f)/A_2(f)$ (Picotti and Carcione 2006).

Using different time windows to define the main pulse leads to different Q values. Toksöz et al. (1979) obtained Q for P waves in Berea sandstone using three periods. We consider four periods as shown in Fig. 2 a and b for sample DO2 (porosity: 16.87%) at 70 MPa differential pressure and full oil saturation (the results are more stable). The quality factor has also been computed with the frequency shift method (Quan and Harris 1997; Picotti and Carcione 2006), and we have obtained similar results. Figure 2 c and d show the frequency spectrum and the spectrum ratio between dolomite and aluminum, respectively. The P wave quality factors were calculated at full water and oil saturations. Figure 3 shows the P wave dissipation factor of the samples at full water and oil saturation as a function of the differential pressure. As pressure increases, attenuation gradually decreases and is higher for oil, whereas water-saturated samples have the lower dissipation. A possible mechanism to explain this behavior is squirt flow between cracks and pores (e.g., Carcione and Gurevich 2011), since the relaxation peak moves to the low frequencies for increasing viscosity, decreasing aspect ratio and crack fraction.

Poroelasticity modeling

The EIAS (equivalent inclusion average stress) model

Assuming a solid background medium containing spherical pores and cracks, the high-frequency bulk and shear moduli of the saturated rock is

$$K_{HF}^{\text{sat}} = K_0 + \frac{\phi\left(K_f - K_0\right)\overline{\gamma}}{1-\phi\left(1-\overline{\gamma}\right)}, \tag{2}$$

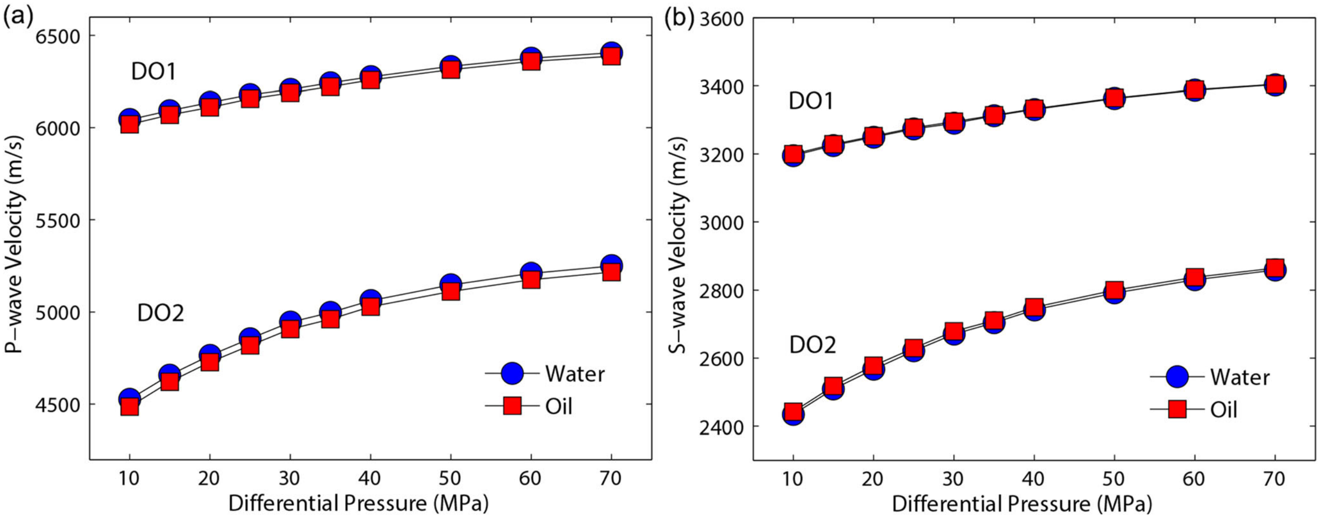

Fig. 1 P and S wave velocities as a function of the differential pressure for the DO1 and DO2 dolomite samples at full water and oil saturation

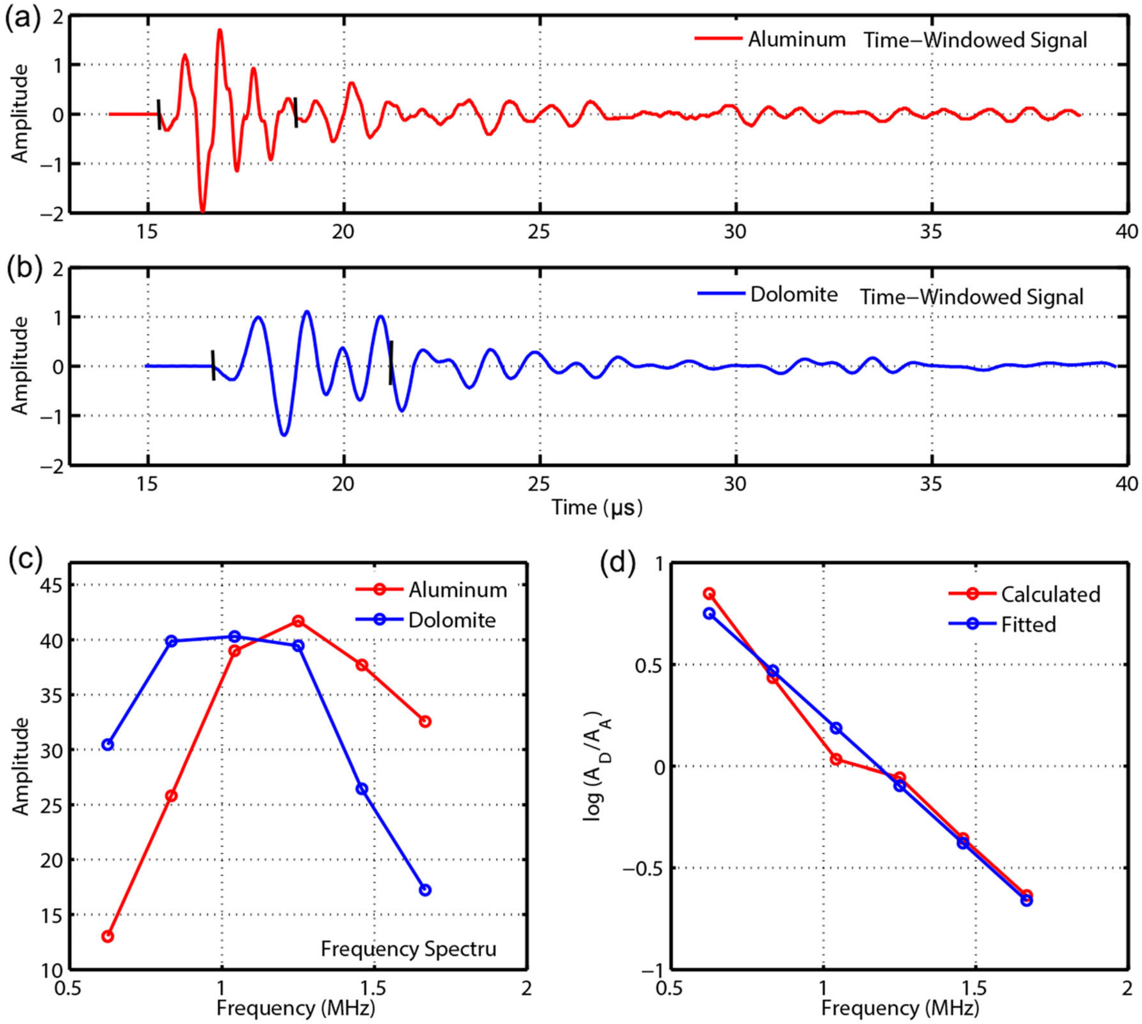

Fig. 2 Sample DO2 (porosity: 16.87%) at 70 MPa differential pressure corresponding to full oil saturation. Waveforms in **a** aluminum and **b** dolomite. The first arrival and the end of the first four periods are indicated. **c** Frequency spectrum and **d** spectral ratio between dolomite and aluminum used in the attenuation analysis

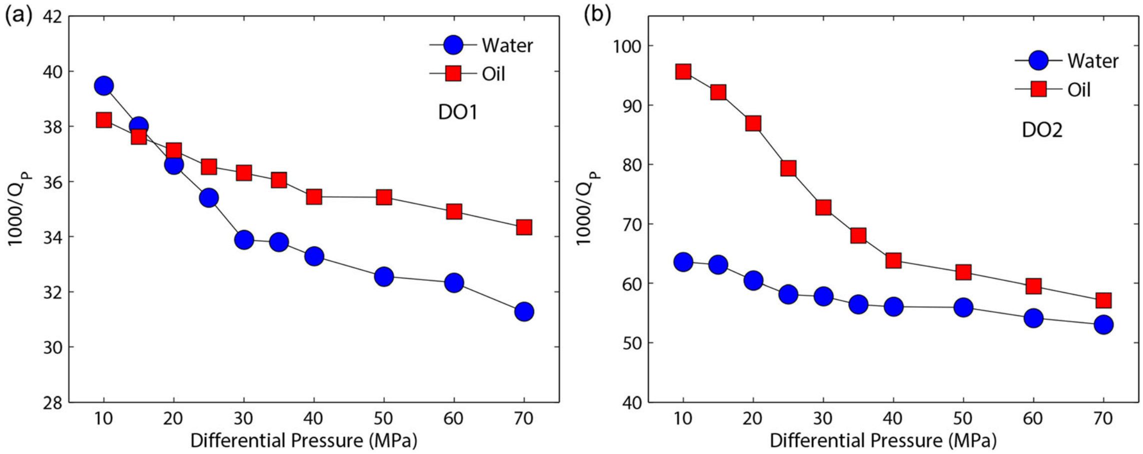

Fig. 3 P wave dissipation factor as a function of differential pressure for the DO1 and DO2 samples at full water and oil saturation

$$G_{HF}^{\text{sat}} = \frac{G_0(1-\phi)}{1-\phi\left(1-\overline{\chi}\right)}, \tag{3}$$

(Endres and Knight 1997), where, ϕ denotes the (equant or stiff) rock porosity, K_0 and G_0 are the bulk and shear moduli of mineral mixture, respectively, K_f is the bulk modulus of fluid,

$$\overline{\gamma} = (1-c)P_1 + cP_2, \overline{\chi} = (1-c)Q_1 + cQ_2, \tag{4}$$

(Berryman 1995; Mavko et al. 2009),

$$P_1 = \frac{K_0 + 4G_0/3}{K_f + 4G_0/3}, P_2 = \frac{K_0}{K_f + \pi a \beta_m}, \tag{5}$$

$$Q_1 = 1 + G_0/\zeta,$$
$$Q_2 = \frac{1}{5}\left[1 + \frac{8G_0}{\pi a(G_0 + 2\beta_m)} + 2\cdot\frac{K_f + 2G_0/3}{K_f + \pi a \beta_m}\right], \tag{6}$$

$$\beta_m = G_0 \cdot \frac{3K_0 + G_0}{3K_0 + 4G_0}, \zeta = \frac{G_0}{6}\cdot\frac{9K_0 + 8G_0}{K_0 + 2G_0}, \tag{7}$$

where a is the crack aspect ratio, Moreover, c and $1 - c$ are the soft pore (crack) and stiff pore fractions. The coefficients P_1 and Q_1 correspond to spherical pores (host) and P_2 and Q_2 to penny-shaped cracks (inclusion phases).

We assume that the crack aspect ratio and fraction are respectively given by

$$a = a_0 \exp[-(p-p_0)/p_a], \quad \text{and } c = c_0 \exp[-(p-p_0)/p_c], \tag{8}$$

(see Appendix A), where p is the differential pressure (confining minus pore pressure), a_0 and c_0 are the values at $p = p_0$ (p_0 is 10 MPa), and p_a and p_c are empirical parameters.

The above equations hold for spherical stiff pores (the aspect ratio: $a_s = 1$). For oblate spheroidal pores with aspect ratio $a_s < 1$, the coefficients in Eq. (4) are

$$P_1 = \frac{1}{3}T_{iijj}, \text{and } Q_1 = \frac{1}{5}\left(T_{ijij} - \frac{1}{3}T_{iijj}\right), \tag{9}$$

where T_{iijj} and T_{ijij} are given in Appendix of Berryman (1980) or in page 189 of Mavko et al. (2009) (the inclusion moduli should be taken equal to zero). For completeness, we report the equations in Appendix B. P_1 and Q_1 in Eqs. (5) and (6) are obtained from (9), whereas P_2 and Q_2 are approximations of (9) for small aspect ratio.

The low frequencies effective moduli, when fluid pressure is equilibrated throughout the pore space, are

$$K_{LF}^{\text{sat}} = K_0 + \frac{\phi K_0\left(K_f - K_0\right)\overline{\gamma}_0}{(1-\phi)\left(K_0 - K_f\right) + \left[K_f + \phi\left(K_0 - K_f\right)\right]\overline{\gamma}_0}, \tag{10}$$

$$G_{LF}^{\text{sat}} = \frac{G_0(1-\phi)}{1-\phi\left(1-\overline{\chi}_0\right)}, \tag{11}$$

where

$$\overline{\gamma}_0 = (1-c)P_{01} + cP_{02}, \overline{\chi}_0 = (1-c)Q_{01} + cQ_{02}, \tag{12}$$

$$P_{01} = 1 + \frac{3K_0}{4G_0}, P_{02} = \frac{K_0}{\pi a \beta_m}, \tag{13}$$

$$Q_{01} = Q_1, Q_{02} = \frac{1}{5}\left[1 + \frac{4G_0}{\pi a}\cdot\frac{G_0 + 8\beta_m}{3\beta_m(G_0 + 2\beta_m)}\right], \tag{14}$$

and

$$P_{0n} = P_n\left(K_f = 0\right), (n = 1, 2),$$
$$Q_{0n} = Q_n\left(K_f = 0\right), (n = 1, 2). \tag{15}$$

The above equations hold for spherical stiff pores. For oblate spheroidal pores with aspect ratio $a_s < 1$, the coefficients in Eq. (12) are obtained from Eqs. (9) and (15).

EIAS-Zener model and seismic properties

The Zener mechanical model (e.g., Carcione 2014) can be used to describe the frequency dependence of dispersion and attenuation, since this model satisfies the Kramers–Kronig relations (Carcione et al. 2018). The minimum quality factors of the dilatational and shear relaxation peaks are

$$Q_{0K}=\frac{2\sqrt{K_{HF}^{sat}K_{LF}^{sat}}}{K_{HF}^{sat}-K_{LF}^{sat}}\text{ and }Q_{0G}=\frac{2\sqrt{G_{HF}^{sat}GK_{LF}^{sat}}}{G_{HF}^{sat}-G_{LF}^{sat}},\qquad(16)$$

respectively, whereas the bulk and shear complex moduli are

$$K(f)=\frac{Q_{0K}+i(f/f_0)\left(\sqrt{1+Q_{0K}^2}+1\right)}{Q_{0K}+i(f/f_0)\left(\sqrt{1+Q_{0K}^2}-1\right)}\cdot K_{LF}^{sat},\qquad(17)$$

$$G(f)=\frac{Q_{0G}+i(f/f_0)\left(\sqrt{1+Q_{0G}^2}+1\right)}{Q_{0G}+i(f/f_0)\left(\sqrt{1+Q_{0G}^2}-1\right)}\cdot G_{LF}^{sat},\qquad(18)$$

where$i=\sqrt{-1}$, f_0 is the frequency of the relaxation peak, such that for $f\rightarrow\infty$, $K\rightarrow K_{HF}^{\text{sat}}$ and for $f\rightarrow 0$,$K\rightarrow K_{LF}^{\text{sat}}$.

The phase velocity and quality factor of the body waves are

$$V=\left[\text{Re}\left\{\frac{1}{v}\right\}\right]^{-1},\qquad(19)$$

and

$$Q=\frac{\text{Re}\{v^2\}}{\text{Im}\{v^2\}},\qquad(20)$$

respectively, where v denotes v_P or v_S, being the frequency-dependent complex P and S wave velocities

$$v_P=\sqrt{\frac{K+4G/3}{\rho}}\text{ and }v_S=\sqrt{\frac{G}{\rho}},\qquad(21)$$

(Carcione 2014), respectively, where ρ is the mass density.

Results

The EIAS model is used to fit the bulk and shear moduli of the rocks as a function of differential pressure, while the frequency dependence of the phase velocities and quality factors are described by the Zener model, which is good approximation to the squirt flow mechanism as shown by Carcione and Gurevich (2011). We consider $K_S = 76.4$ GPa and $\mu_s = 49.7$ GPa (Mavko et al. 2009), and the fluid properties are obtained from Batzle and Wang (1992). The density and stiffness moduli of water and oil (kerosene) are shown the Table 2.

The bulk and shear moduli of the rocks are obtained at the unrelaxed state experimentally, and calculated as

$$K_{\exp}=\rho\left(V_P^2-\frac{4}{3}V_S^2\right),\text{ and }G_{\exp}=\rho V_S^2,\qquad(22)$$

First, we consider the data for $p = p_0$=10 MPa and obtain $a = a_0$, and $c = c_0$, spanning the crack attributes in the range $a = [0, 0.01]$ and $c = [0, 0.3]$ to satisfy

$$\left(\left|1-\frac{K_{HF}^{sat}(a_0,c_0)}{K_{\exp}(p_0)}\right|+\left|1-\frac{G_{HF}^{sat}(a_0,c_0)}{G_{\exp}(p_0)}\right|\right)\le\varepsilon_0,\qquad(23)$$

where ε_0 is the error, $K_{HF}^{\text{sat}}(a_0\ ,c_0)$ and $G_{HF}^{\text{sat}}(a_0\ ,c_0)$ are the predicted bulk and shear moduli by the EIAS model, and $K_{\exp}(p_0)$ and $G_{\exp}(p_0)$ are the experimental bulk and shear moduli at p_0, respectively.

Then, we obtain p_a and p_c by replacing a_0 and c_0 into eq. (8), and assuming that p_a and p_c are in the range [0, 200] MPa to satisfy

$$\sum_{i=0}^{9}\left(\left|1-\frac{K_{HF}^{sat}(a_i,c_i)}{K_{\exp}(p_i)}\right|+\left|1-\frac{G_{HF}^{sat}(a_i,c_i)}{G_{\exp}(p_i)}\right|\right)\le\varepsilon,\qquad(24)$$

where ε is the error, $K_{HF}^{\text{sat}}(a_i\ ,c_i)$ and $G_{HF}^{\text{sat}}(a_i\ ,c_i)$ are the predicted bulk and shear moduli by the EIAS model, where i from 0 to 9 corresponds to pressures 10, 15, 20, 25, 30, 35, 40, 50, 60, and 70 MPa, and $K_{\exp}(p_i)$ and $G_{\exp}(p_i)$ are the experimental bulk and shear moduli at p_i, respectively. Thereafter, we obtain a and c from Eq. (8).

We assume that the stiff pores are spherical, i.e., $a_s = 1$, but also analyze the cases $a_s = 0.8$, 0.6, 0.4, 0.2, 0.15, 0.1, and 0.08. Figure 4 shows the results for the DO2 sample saturated with the different fluids, i.e., the bulk and shear moduli as a function of the differential pressure. For $0.2 \leqq a_s \leqq 1$, the results are very similar and agree with the experimental data. For $a_s = 0.15$, 0.1, and 0.08, the curves deviate from the data, indicating that the spherical assumption is acceptable. The results are shown in Fig. 5 and summarized in Table 2, where it can be seen that the shear modulus is not affected as the bulk modulus and the error less than 0.022.

Figures 6 and 7 show the crack aspect ratio and fraction as a function of the differential pressure, respectively. Both attributes decrease with increasing pressure and are higher when the rock is saturated with water and lower at full oil saturation, since cracks filled with oil close first at the same pressure, followed by water. This can be interpreted as the effect of the fluid bulk modulus. Moreover, we obtain the crack porosity and density by using Eqs. (34) and (35), respectively. The trend of the crack porosity and density decreases with increasing differential pressure, in agreement with Duan et al. (2018). The crack aspect ratio and fraction in the DO2 sample is higher, compared with the DO1 sample; both attributes seem to increase with increasing porosity.

Table 2 Fluid properties and crack attributes

Sample	Fluid	Fluid density (kg/m^3)	K_f (GPa)	a_0	c_0	ε_0	p_a (MPa)	p_c (MPa)
DO1	Water	934	2.12	0.0013	0.074	0.010	32.6	27
	Kerosene	800	1.25	0.0009	0.050	0.014	34	28.6
DO2	Water	934	2.12	0.0052	0.204	0.022	131	51.6
	Kerosene	800	1.25	0.0030	0.121	0.013	191.6	56

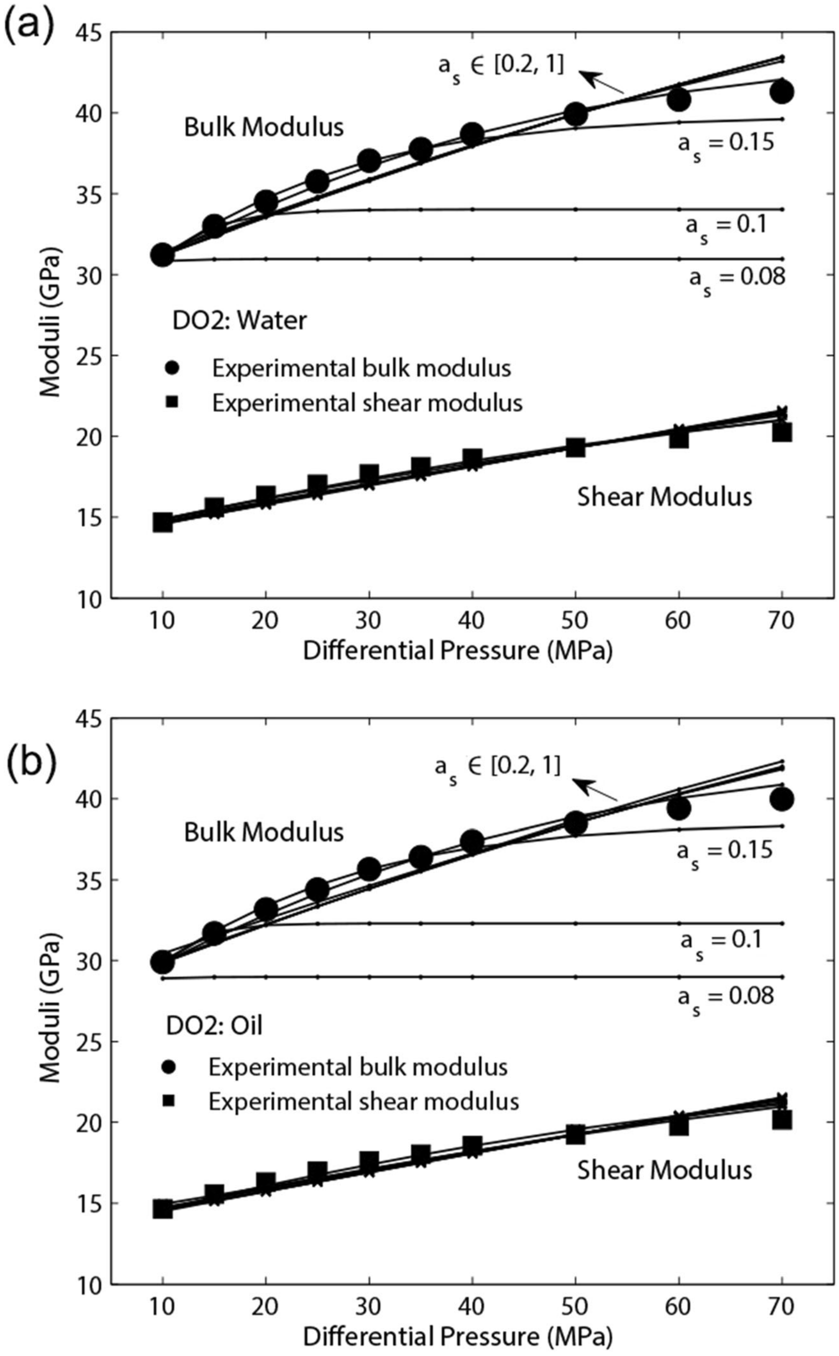

Fig. 4 Bulk and shear moduli as a function of the differential pressure for the DO2 sample at full water and oil saturation. The solid lines are predictions of the EIAS model with different stiff-pore aspect ratios

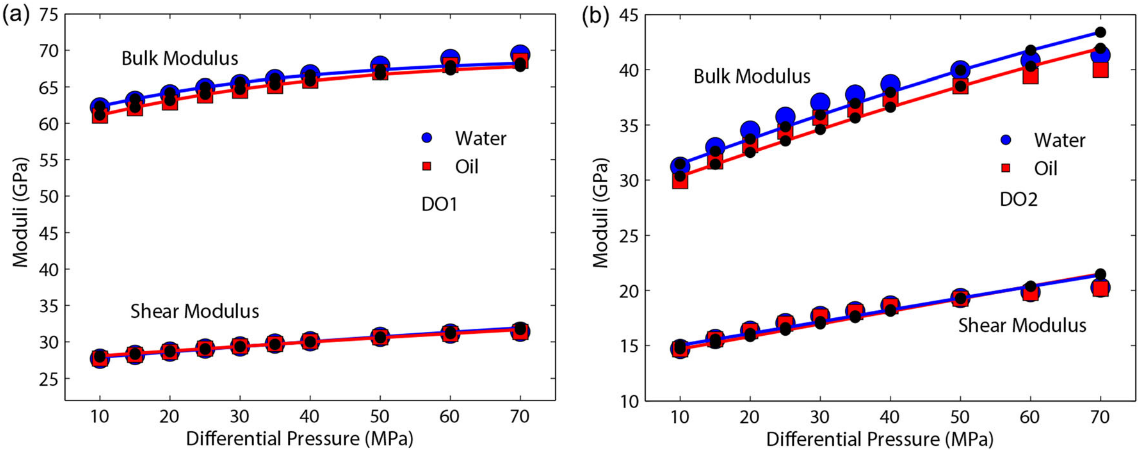

Fig. 5 Bulk and shear moduli as a function of the differential pressure for the DO1 and DO2 samples at full water and oil saturation. The solid lines are predictions of the EIAS model with spherical stiff pores ($a_s = 1$)

Next, we use the EIAS-Zener model to obtain the phase velocity and quality factor as a function of frequency, where the values of f_0 are chosen to fit the experimental P wave velocity and inverse quality factor (see Fig. 8). For one Zener model, the quality factor at the experimental frequency is (Carcione 2014)

$$Q_1 = \frac{1+\omega_1^2\tau_\varepsilon\tau_\sigma}{\omega_1(\tau_\varepsilon - \tau_\sigma)}, \tag{25}$$

where τ_ε and τ_σ are relaxation times and ω_1 is the experimental angular frequency. The model has a relaxation peak at $\omega_0 = 1/\tau_0$, where

$$\tau_0 = \sqrt{\tau_\varepsilon\tau_\sigma}, \tag{26}$$

Thus,

$$\tau_\varepsilon - \tau_\sigma = \frac{1+\omega_1^2/\omega_0^2}{\omega_1 Q_1}, \tag{27}$$

The quality factor at the relaxation peak frequency is

$$Q_0 = \frac{1+\omega_0^2\tau_\varepsilon\tau_\sigma}{\omega_0(\tau_\varepsilon - \tau_\sigma)}, \tag{28}$$

Substituting $f_0 = 2\pi\omega_0, f_1 = 2\pi\omega_1$ (f_1 is the experimental frequency) into Eqs. (26), (27), and (28), we obtain

$$f_0^2 - 2qf_1f_0 + f_1^2 = 0, \tag{29}$$

where $q = Q_1/Q_0$, moreover, the solution is

$$f_0 = \left(q \pm \sqrt{q^2 - 1}\right)f_1 \tag{30}$$

The solution providing the best fit of $K_{\rm exp}$ with $K_{HF}^{\rm sat}$ by using Eqs. (23) and (24) is that corresponding to the minus sign.

The relaxation frequency for oil is slightly smaller than that of water, in agreement with the squirt flow theory, since the location of the characteristic frequency is inversely proportional to viscosity (see Eq. 19 in Carcione and Gurevich (2011)).

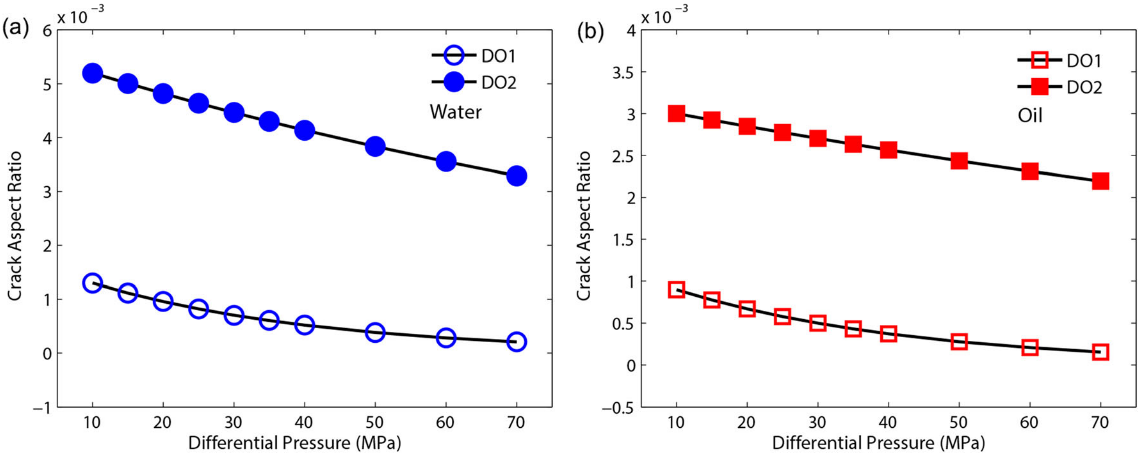

Fig. 6 Crack aspect ratio as a function of the differential pressure for the DO1 and DO2 samples at full water and oil saturation

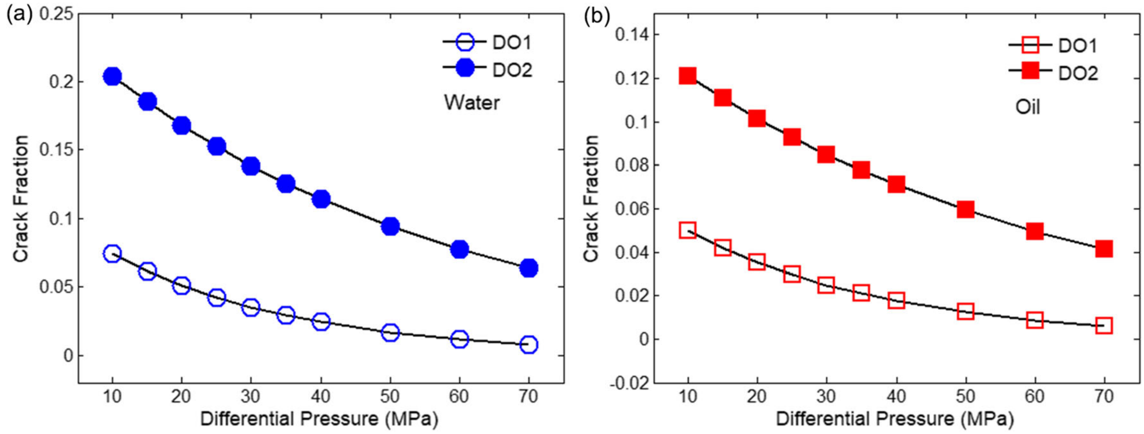

Fig. 7 Crack fraction as a function of the differential pressure for the DO1 and DO2 samples at full water and oil saturation

Conclusions

Rock pore structure, porosity, fluid type, and pressure significantly affect acoustic wave propagation. Porosity is mainly formed by round (stiff) pores and to a much lesser extent by cracks (soft pores); the latter is described by the crack aspect ratio and fraction (or crack porosity). However, variations in these properties have a greater effect than variations of those corresponding to equant (or stiff) pores. We have performed ultrasonic measurements on two dolomite samples with varying differential pressure and fluid type (water and oil). The soft-pore (crack) properties and anelasticity of dolomites are then analyzed by using the EIAS-Zener model. We obtain the crack aspect ratio and fraction as a function of pressure, and the phase velocities and quality factors as a function of frequency. The results show that the cracks close first when the

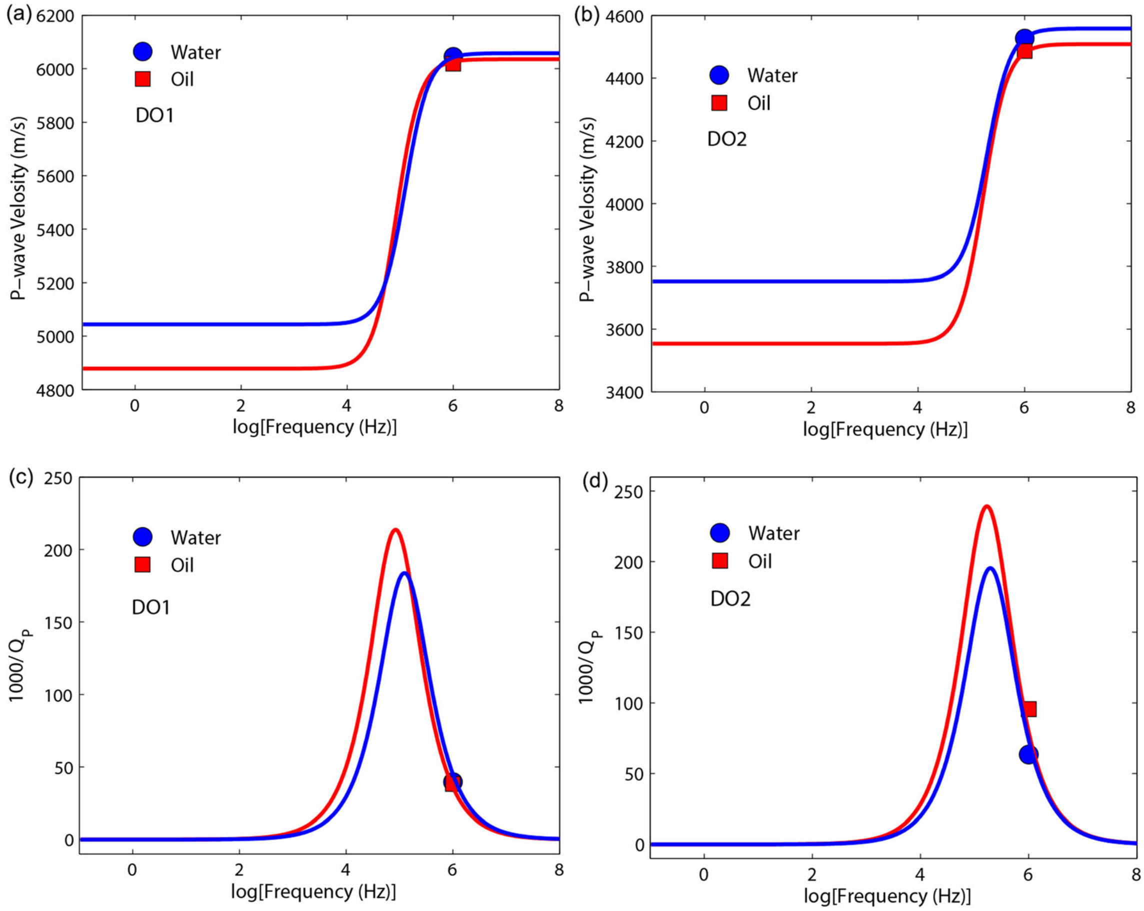

Fig. 8 Measured P wave velocities and dissipation factor compared with the EIAS-Zener model predictions for samples DO1 and DO2 at full water and oil saturation. The symbols correspond to the experimental data

fluid is oil, followed by water. As differential pressure increases, the crack aspect ratio and fraction decrease, as expected. Match of the experimental quality factor allows us to obtain the location of the relaxation peak, presumably interpreted as a result of squirt flow between pores of cracks.

Funding information This work is supported by the Cultivation Program of the "111" Plan of China (BC2018019), Jiangsu Innovation and Entrepreneurship Plan, Specially-Appointed Professor Program of Jiangsu Province, and the National Natural Science Foundation of China (grant no. 41974123, 41704109).

Appendix A

Previous studies show that the crack density has the form (Zhang et al. 2019; Duan et al. 2018)

$$\Gamma(P) = \Gamma_0 e^{-P/\widehat{p}}, \tag{31}$$

where Γ_0 is the initial crack density at zero differential pressure, $\widehat{p}$ is a compaction coefficient, and P is the differential pressure. Shapiro (2003) and Yin et al. (2017) relate crack porosity and differential pressure,

$$\phi_c = \phi_{c0}\exp(-\theta_c C_{drs} P), \tag{32}$$

$$\theta_c = \frac{1}{C_{drs}}\frac{\partial C_{dr}}{\partial \phi_c}, \tag{33}$$

where ϕ_c is the crack porosity, ϕ_{c0} is the crack porosity at zero differential pressure, $C_{dr} = 1/K_{dr}$ is the dry-rock compressibility, K_{dr} is the dry bulk modulus, C_{drs} is the compressibility of the dry rock with the compliant pores closed. Therefore, the relation between crack fraction and differential pressure is

$$c = \phi_c/\phi = \frac{\phi_{c0}}{\phi}\exp(-\theta_c C_{drs} P), \tag{34}$$

because

$$\Gamma(P) = \frac{3\phi c}{4\pi a}, \tag{35}$$

and

$$a = \frac{3\phi c}{\Gamma(P)4\pi}, \tag{36}$$

Substituting Eqs. (31) and (34) into (36) yields

$$a = \frac{3\phi_{c0}}{\Gamma_0 4\pi}\exp\left(\left(1/\widehat{p}-\theta_c C_{drs}\right)P\right), \tag{37}$$

Both a and c have an exponential dependence on differential pressure. Therefore, we assume that the crack aspect ratio and fraction are respectively given by eq. (8).

Appendix B

The coefficients P and Q for ellipsoidal inclusions of arbitrary aspect ratio are given by

$$P = \frac{1}{3}T_{iijj}, \text{ and } Q = \frac{1}{5}\left(T_{ijij}-\frac{1}{3}T_{iijj}\right), \tag{38}$$

where the strain within the ellipsoidal inclusion and the uniform far-field strain field are related by the tensor T_{ijkl} (Wu 1966). Berryman (1980) gives the expressions

$$T_{iijj} = \frac{3F_1}{F_2}, \text{ and } T_{ijij}-\frac{1}{3}T_{iijj} = \frac{2}{F_3}+\frac{1}{F_4}+\frac{F_4F_5+F_6F_7-F_8F_9}{F_2F_4}, \tag{39}$$

where

$$\begin{aligned}
F_1 &= 1+A\left[\frac{3}{2}(ff+\theta)-R\left(\frac{3}{2}ff+\frac{5}{2}\theta-\frac{4}{3}\right)\right]\\
F_2 &= 1+A\left[1+\frac{3}{2}(ff+\theta)-\frac{1}{2}R(3ff+5\theta)\right]+B(3-4R)\\
&\quad +\frac{1}{2}A(A+3B)(3-4R)\left[ff+\theta-R\left(ff-\theta+2\theta^2\right)\right]\\
F_3 &= 1+A\left[1-\left(ff+\frac{3}{2}\theta\right)+R(ff+\theta)\right]\\
F_4 &= 1+\frac{1}{4}A[ff+3\theta+R(ff-\theta)]\\
F_5 &= A\left[-ff+R\left(ff+\theta-\frac{4}{3}\right)\right]+B\theta(3-4R),\\
F_6 &= 1+A[1+ff-R(ff+\theta)]+B(1-\theta)(3-4R)\\
F_7 &= 2+\frac{1}{4}A[3ff+9\theta-R(3ff+5\theta)]+B\theta(3-4R)\\
F_8 &= A\left[1-2R+\frac{1}{2}ff(R-1)+\frac{1}{2}\theta(5R-3)\right]+B(1-\theta)(3-4R)\\
F_9 &= A[(R-1)ff-R\theta]+B\theta(3-4R)
\end{aligned} \tag{40}$$

with A, B, and R are

$$A = \frac{G_i}{G_0}-1, B = \frac{1}{3}\left(\frac{K_i}{K_0}-\frac{G_i}{G_0}\right) \text{ and } R = \frac{(1-2\nu_0)}{2(1-\nu_0)}, \tag{41}$$

The functions θ and ff for oblate spheroids are

$$\theta = \frac{a}{(1-a^2)^{3/2}}\left[\cos^{-1}a-a\left(1-a^2\right)^{1/2}\right] \text{ and } ff = \frac{a^2}{(1-a^2)}(3\theta-2), \tag{42}$$

References

Ba J, Zhao JG, Carcione JM, Huang XX (2016) Compressional wave dispersion due to rock matrix stiffening by clay squirt flow. Geophys Res Lett 43:6186–6195. https://doi.org/10.1002/2016GL069312

Ba J, Xu W, Fu L, Carcione JM, Zhang L (2017) Rock anelasticity due to patchy-saturation and fabric heterogeneity: A double double-porosity model of wave propagation. Journal of Geophysical

Research-solid earth 122(3):1949–1976. https://doi.org/10.1002/2016JB013882

Ba J, Ma RP, Carcione JM, Picotti S (2019) Ultrasonic wave attenuation dependence on saturation in tight oil siltstones. J Pet Sci Eng 179: 1114–1122. https://doi.org/10.1016/j.petrol.2019.04.099

Batzle M, Wang Z (1992) Seismic properties of pore fluids. Geophysics 57(11):1396–1408. https://doi.org/10.1190/1.1443207

Berryman JG (1980) Long-wavelength propagation in composite elastic media. J Acoust Soc Am 68:1809–1831. https://doi.org/10.1121/1.385172

Berryman JG (1995) Mixture theories for rock properties. A handbook of physical constants Washington, D C: American Geophysical Union, 205–228. https://doi.org/10.1029/RF003p0205

Carcione JM (2014) Wave fields in real media. Theory and numerical simulation of wave propagation in anisotropic, anelastic, porous and electromagnetic media, Elsevier. (third edition, extended and revised). https://www.elsevier.com/books/wave-fields-in-real-media/carcione/978-0-08-099999-9

Carcione JM, Gurevich B (2011) Differential form and numerical implementation of Biot's poroelasticity equations with squirt dissipation. Geophysics 76:N55–N64. https://doi.org/10.1190/geo2010-0169.1

Carcione JM, Cavallini F, Ba J, Cheng W, Qadrouh A (2018) On the Kramers-Kronig relations. Rheol Acta. https://doi.org/10.1007/s00397-018-1119-3

Cheng CH, Toksöz MH (1979) Inversion of seismic velocities for the pore aspect ratio spectrum of a rock. J Geophys Res 84(B13):7533–7543. https://doi.org/10.1029/JB084iB13p07533

Cheng W, Carcione JM, Qadrouh A, Alajmi M, Ba J (2020) Rock anelasticity, pore geometry and the Biot-Gardner effect. Rock Mech Rock Eng. https://doi.org/10.1007/s00603-020-02155-7

Cleary MP (1978) Elastic and dynamic response regimes of fluid-impregnated solids with diverse microstructures. Int J Solids Struct 14:795–819. https://doi.org/10.1016/0020-7683(78)90072-0

Duan C, Deng J, Li Y, Lu Y, Tang Z, Wang X (2018) Effect of pore structure on the dispersion and attenuation of fluid-saturated tight sandstone. J Geophys Eng 15(2):449–460

Endres A, Knight R (1997) Incorporating pore geometry and fluid pressure communication into modeling the elastic behavior of porous rock. Geophysics 62(1):106–117. https://doi.org/10.1190/1.1444110

Gassmann F (1951) Elastic waves through a parking of spheres. Geophysics 16:673–685. https://doi.org/10.1190/1.1437718

Guo M, Fu L (2007) Stress associated coda attenuation from ultrasonic waveform measurements. Geophys Res Lett 34:L09307. https://doi.org/10.1029/2007gl029582

Guo M, Fu L, Ba J (2009) Comparison of stress-associated coda attenuation and intrinsic attenuation from ultrasonic measurements. Geophys J Int 178:447–456. https://doi.org/10.1111/j.1365-246X.2009.04159.x

Izumotani S, Onozuka S (2013) Elastic moduli and the aspect ratio spectrum of rock using simulated annealing. Geophys Prospect 61:489–504. https://doi.org/10.1111/1365-2478.12003

Jones TD (1986) Pore fluids and frequency-dependent wave propagation in rocks. Geophysics 51:1939–1953. https://doi.org/10.1190/1.1442050

King MS, Marsden JR (2002) Velocity dispersion between ultrasonic and seismic frequencies in brine-saturated reservoir sandstones. Geophysics 67(1):254–258. https://doi.org/10.1190/1.1451700

Mavko G, Nolen-Hoeksema R (1994) Estimating seismic velocities at ultrasonic frequencies in partially saturated rocks. Geophysics 59(2):252–258. https://doi.org/10.1190/1.1443587

Mavko G, Mukerji T, Dvorkin J (2009) The rock physics handbook. Cambridge Univ Press

Müller TM, Gurevich B, Lebedev M (2010) Seismic wave attenuation and dispersion resulting from wave-induced flow in porous rocks-a review. Geophysics 75(5):75A147–175A164. https://doi.org/10.1190/1.3463417

Murphy WF (1984) Sonic and ultrasonic velocities: theory versus experiment. Geophys Res Lett 12:85–88. https://doi.org/10.1029/GL012i002p00085

Picotti S, Carcione JM (2006) Estimating seismic attenuation (Q) in the presence of random noise. J Seism Explor 15(2):165–181

Quan Y, Harris JM (1997) Seismic attenuation tomography using the frequency shift method. Geophysics 62:895–905. https://doi.org/10.1190/1.1444197

Shapiro SA (2003) Elastic piezosensitivity of porous and fractured rocks. Geophysics 68(2):482–486

Toksöz MN, Cheng CH, Aytekin T (1976) Velocities of seismic waves in porous rocks. Geophysics 41(4):621–645. https://doi.org/10.1190/1.1440639

Toksöz MN, Johnston DH, Timur A (1979) Attenuation of seismic waves in dry and saturated rocks:I. Laboratory measurements. Geophysics 44:681–690. https://doi.org/10.1190/1.1440969

Wu TT (1966) The effect of inclusion shape on the elastic moduli of a two-phase material. Int J Solids Struct 2(1):1–8. https://doi.org/10.1016/0020-7683(66)90002-3

Yin H, Zhao J, Tang G, Zhao L, Ma X, Wang S (2017) Pressure and fluid effect on frequency-dependent elastic moduli in fully saturated tight sandstone. J Geophys Res Solid Earth 122:8925–8942. https://doi.org/10.1002/2017JB014244

Zhang L, Ba J, Fu L, Carcione JM, Cao C (2019) Estimation of pore microstructure by using the static and dynamic moduli. Int J Rock Mech Min Sci 113:24–30. https://doi.org/10.1016/j.ijrmms.2018.11.005